## Supplementary information

# A liquid-metal foam pressure sensor for machine-learning-enabled handwritten digit recognition and user authentication

*Jiali Wang[1], Yongjiang Wang[2], Fawang He[1], Ruihan Lu[2], Hao Bai[1], Zhenguo Liu[1,2,*], Shuhao Cai[2,*], Wei Huang[1,3,*]*

1 Frontiers Science Center for Flexible Electronics & Institute of Flexible Electronics, Northwestern Polytechnical University, Xi'an 710072, China

2 Key Laboratory of Flexible Electronics of Zhejiang Province, Ningbo Institute of Northwestern Polytechnical University, 218 Qingyi Road, Ningbo 315103, China

3 Key Laboratory of Flexible Electronics and Institute of Advanced Materials, Nanjing Tech University, Nanjing 211800, China

* Corresponding authors: Zhenguo Liu (iamzgliu@nwpu.edu.cn); Shuhao Cai (caishuhao@mail.ru); Wei Huang (vc@nwpu.edu.cn)

**This file includes:**

• Supplementary Figure 1. Optical photographs of pristine LM and SaLM droplets.

• Supplementary Figure 2. TEM images and EDS elemental mapping of SaLM droplets.

• Supplementary Figure 3. FTIR spectrum of SaLM droplets.

• Supplementary Figure 4. High-resolution O 1s XPS spectra of SaLM droplets prepared with different Sa concentrations.

• Supplementary Table 1. Relative proportions of oxygen-containing species in SaLM droplets prepared with different Sa concentrations.

• Supplementary Figure 5. FTIR spectra of SaLM droplets prepared with different Sa concentrations.

• Supplementary Figure 6. Schematic illustration of the transition from interacting hydroxyl-dominated to free hydroxyl-dominated states.

• Supplementary Figure 7. The relationship between the contact angle and the surface tension.

• Supplementary Figure 8. Optical photograph of SaLM/SeCNT droplets.

• Supplementary Figure 9. XRD patterns of CNT, LM, SaLM, SeCNT and SaLM/SeCNT.

• Supplementary Figure 10. Depth-dependent high-resolution Ga 2p and O 1s XPS spectra of SaLM/SeCNT after ion-beam etching.

• Supplementary Figure 11. TEM images of SaLM/SeCNT droplets with different SeCNT ratios.

• Supplementary Figure 12. Conductivity evolution of SeCNT and SaLM/SeCNT as a function of SeCNT concentration.

• Supplementary Table 2. Comparison of this work with previously reported liquid metal based inks.

• Supplementary Figure 13. Interfacial-interaction and composition characterization of SaLM/SeCNT droplets with different SeCNT ratios.

• Supplementary Figure 14. FTIR spectra comparison among Sa, SaLM and SaLM/SeCNT.

• Supplementary Figure 15. Schematic illustration of the PMMA-supported melamine-foam architecture.

• Supplementary Figure 16. SEM images of melamine foams impregnated with different PMMA concentrations.

• Supplementary Figure 17. Compressive stress-strain curves of melamine foams treated with different PMMA concentrations.

• Supplementary Figure 18. SEM image of SaLM/SeCNT-loaded melamine foam without PMMA treatment.

• Supplementary Figure 19. XPS survey spectra of PMMA foam and SaLM/SeCNT/PMMA foam.

• Supplementary Figure 20. FTIR spectra of PMMA foam, SaLM/SeCNT droplets and SaLM/SeCNT/PMMA foam.

• Supplementary Figure 21. Reproducibility of the SaLM/SeCNT/PMMA foam pressure sensors.

• Supplementary Table 3. Performance comparison between recently reported liquid metal based pressure sensors and this work.

• Supplementary Figure 22. Pressure-response performance of the SaLM/SeCNT-loaded melamine-foam pressure sensor without PMMA carrier films.

• Supplementary Figure 23. Cyclic response of the SaLM/SeCNT-loaded melamine-foam pressure sensor without PMMA carrier films.

• Supplementary Figure 24. On-body motion monitoring using the SaLM/SeCNT/PMMA foam pressure sensor.

• Supplementary Figure 25. Full Morse-code chart used for tactile encoding.

• Supplementary Figure 26. Authentication reliability and computational cost of the machine-learning models under the same hardware setting.

• Supplementary Figure 27. Threshold-dependent FAR and FRR curves for SVM, 1D-CNN and CNN-LSTM.

• Supplementary Figure 28. Performance evaluation of digit recognition and user authentication under distinct impostor attack scenarios.

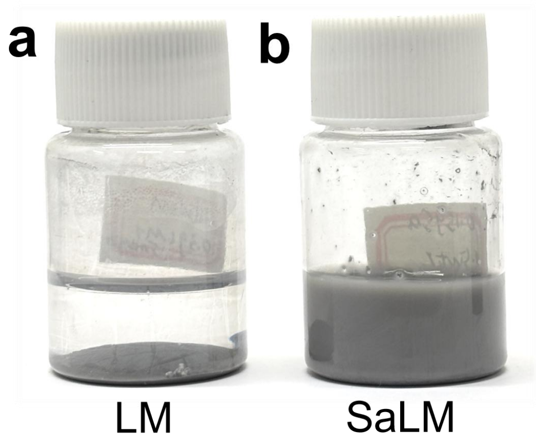


**Supplementary Figure 1. Optical photographs of pristine LM and SaLM droplets.**

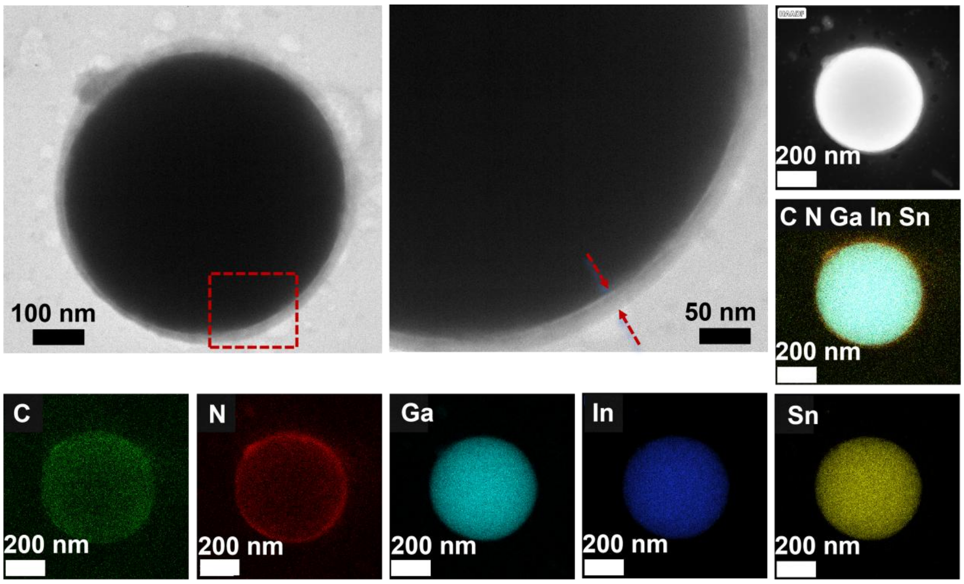


**Supplementary Figure 2. TEM images and EDS elemental mapping of SaLM droplets.**

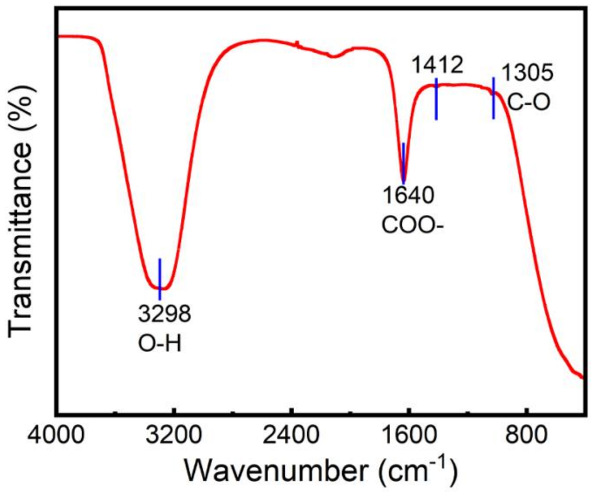


**Supplementary Figure 3. FTIR spectrum of SaLM droplets.**

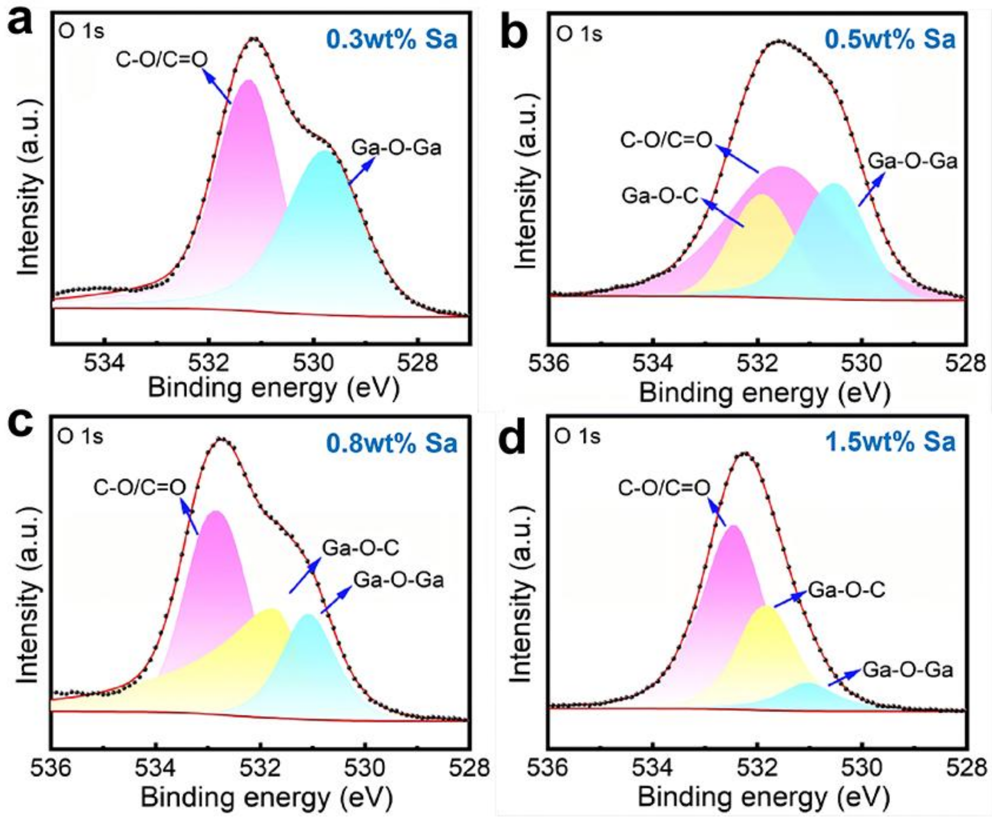


**Supplementary Figure 4. High-resolution O 1s XPS spectra of SaLM droplets prepared with different Sa concentrations. a** 0.3wt%. **b** 0.5wt%. **c** 0.8wt%. d 1.5wt%.

**Supplementary Table 1. Relative proportions of oxygen-containing species in SaLM droplets prepared with different Sa concentrations.**

| Sample | Name | FWHM (eV) | Area (P) CPS. ev | Atomic (%) |
|---|---|---|---|---|
| 0.3wt% SaLM | Ga-O-Ga | 529.8 | 168199.67 | 46.76 |
| | Ga-O-C | / | / | / |
| 0.5wt% SaLM | Ga-O-Ga | 530.5 | 82532.89 | 28.10 |
| | Ga-O-C | 531.9 | 61885.40 | 21.10 |
| 0.8wt% SaLM | Ga-O-Ga | 531.1 | 115459.81 | 38.62 |
| | Ga-O-C | 531.8 | 115526.87 | 38.61 |
| 1.5wt% SaLM | Ga-O-Ga | 531.0 | 32084.74 | 12.07 |
| | Ga-O-C | 531.8 | 97690.66 | 36.76 |

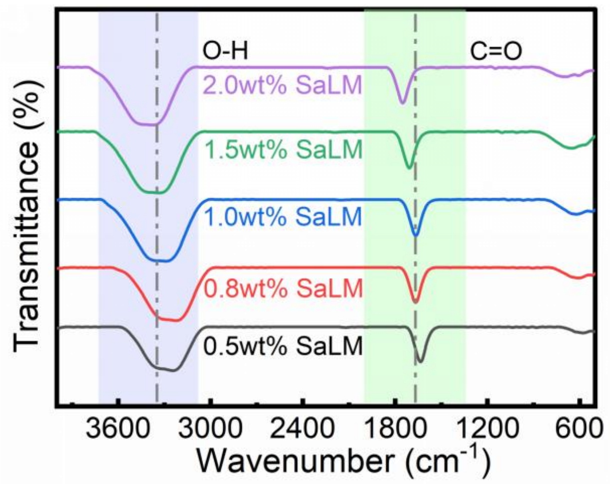


**Supplementary Figure 5. FTIR spectra of SaLM droplets prepared with different Sa concentrations.**

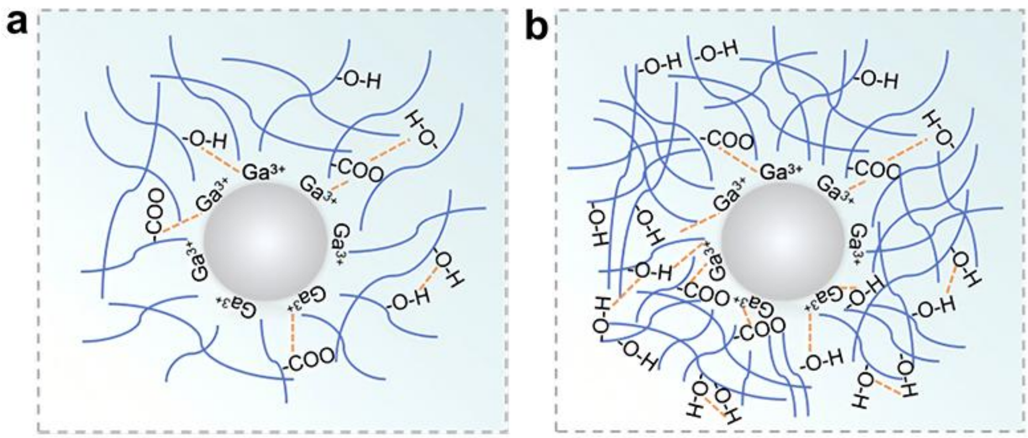


**Supplementary Figure 6. Schematic illustration of the transition from interacting hydroxyl-dominated to free hydroxyl-dominated states.**

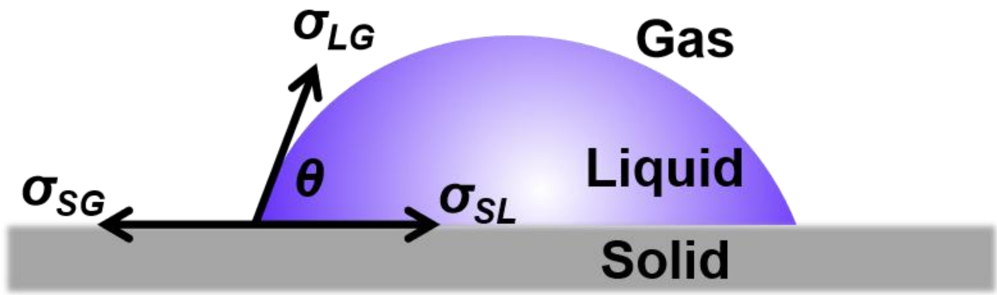


**Supplementary Figure 7. The relationship between the contact angle and the surface tension.**

The relationship between the contact angle and the surface tension can be described by the following two equations:

$$\sigma_{SG} = \sigma_{SL} + \sigma_{LG}\cos\theta \tag{1}$$

$$W_{SL} = \sigma_{LG} + \sigma_{SG} - \sigma_{SL} \tag{2}$$

where $\sigma_{SG}$, $\sigma_{SL}$, and $\sigma_{LG}$ are the surface tensions of solid–gas interface, solid–liquid interface, and liquid–gas interface, θ is the contact angle. Equation (2) indicates the relationship between the adhesion work and the surface tension. Combining Eqs. (1) and (2) together, adhesion work (WSL) can be described by Equation (3), which is called the Young-Dupre Equation:

$$W_{SL} = \sigma_{LG}\left(1 + \cos\theta\right) \tag{3}$$

According to the previous study, the σLG of GaInSn is 500 mN/m.

**Supplementary Figure 8. Optical photograph of SaLM/SeCNT droplets.**

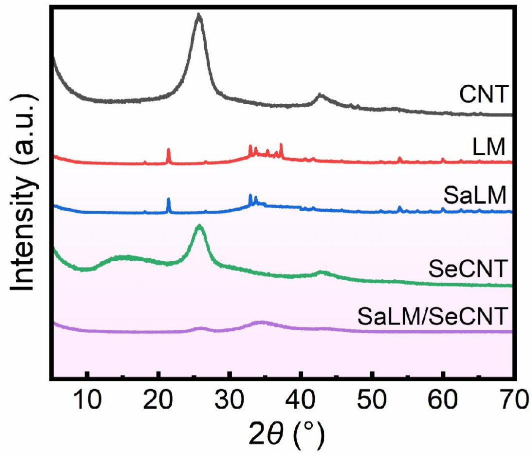


**Supplementary Figure 9. XRD patterns of CNT, LM, SaLM, SeCNT and SaLM/SeCNT.**

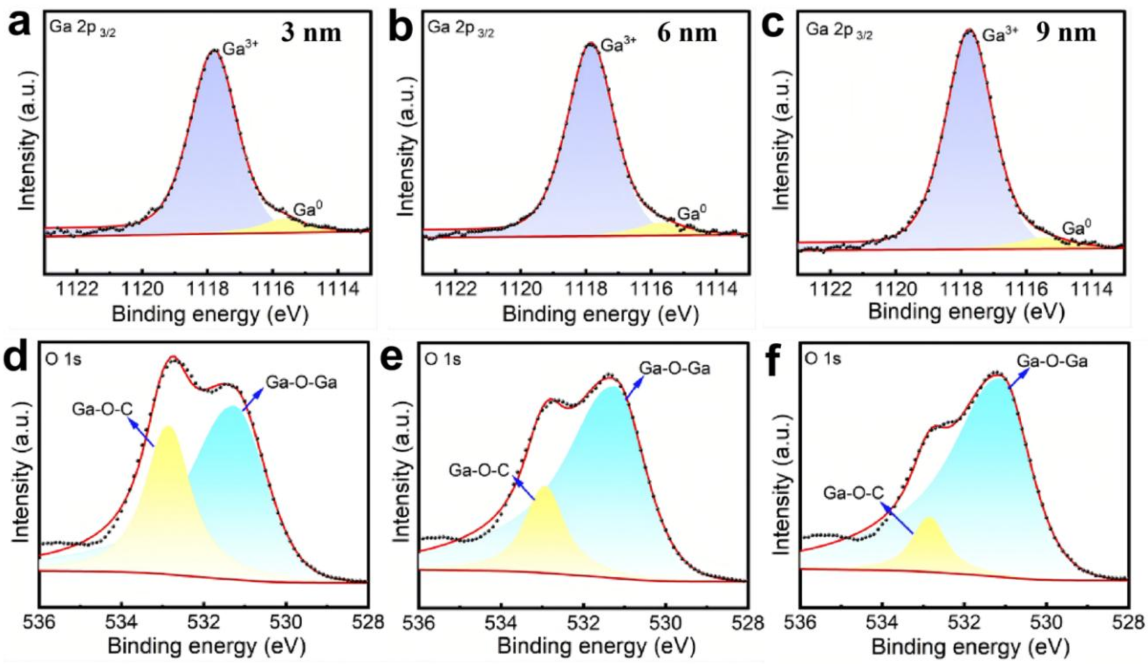


**Supplementary Figure 10. Depth-dependent high-resolution Ga 2p and O 1s XPS spectra of SaLM/SeCNT after ion-beam etching at 3, 6 and 9 nm.**

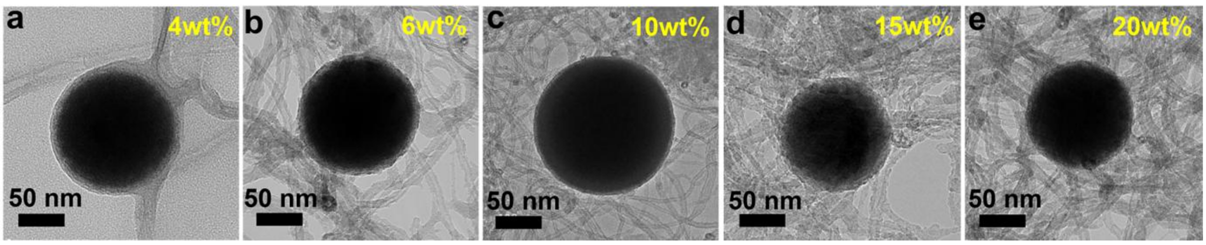


**Supplementary Figure 11. TEM images of SaLM/SeCNT droplets with different SeCNT ratios, showing incomplete nanotube coverage at low loading and aggregation at excessive loading.**

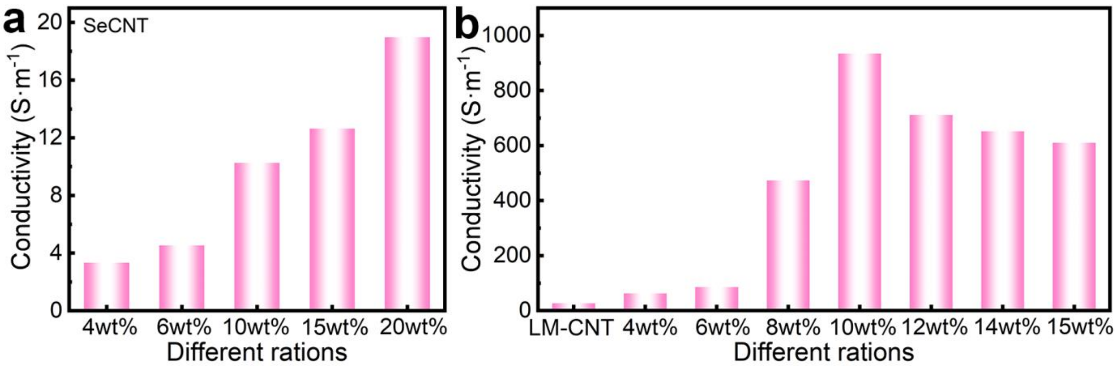


**Supplementary Figure 12. Conductivity evolution of SeCNT and SaLM/SeCNT as a function of SeCNT concentration. a** Conductivity of SeCNT at different concentrations. **b** Conductivity of SaLM/SeCNT at different SeCNT ratios.

**Supplementary Table 2. Comparison of this work with previously reported liquid metal based inks.**

| Materials | Substrate | Solution | Strategies | Conductivity ($S \cdot m^{-1}$) | Sintering | Ref. |
|---|---|---|---|---|---|---|
| $SiO_2$, EGaIn | Ecoflex, Paper | - | Magnetic stirrer | $6.53*10^6$ | Stir | 1 |
| PEDOT: PSS, HPPU, EGaIn | Glass | Ethanol | Orbital shaker | $2.09*10^5$ | Thermal treatment | 2 |
| Sodium alginate, EGaIn | TPU | Deionized water | Ultrasonic processing | $2.0*10^5$ | Not need | 3 |
| PVP, EGaIn | A4 paper, PET, glass slides, etc. | Ethanol | Probe sonication | $6.803*10^4$ | Mechanical | 4 |
| COL Hydrogel, CNTs, EGaIn | - | - | Ultrasonic | 50.75 | - | 5 |
| Sodium alginate, CNTs, EGaIn | Microstructures and Bumps | Deionized water | Ultrasonic | 500 | Not need | 6 |
| Sodium alginate, EGaIn | Porous foam | Deionized water | Ultrasonic | 12 | Mechanical | 7 |
| Sodium alginate, CNTs, EGaIn | Porous foam | Deionized water | Probe sonication | 900 | Not need | This work |

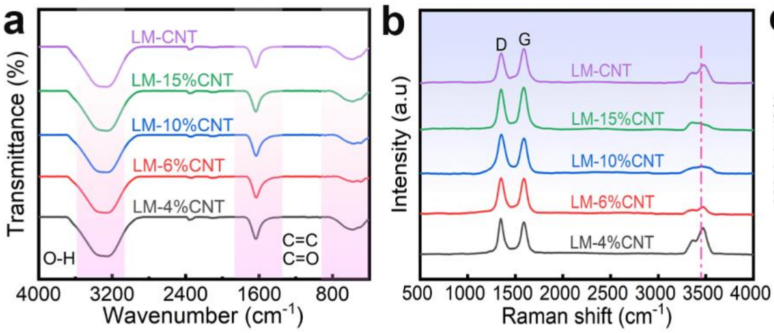


**Supplementary Figure 13. Interfacial-interaction and composition characterization of SaLM/SeCNT droplets with different SeCNT ratios. a** FTIR spectra showing hydroxyl- and carboxyl-related band shifts associated with hydrogen-bonding/electrostatic interactions between SeCNT and the alginate shell. **b** Raman spectra and $I_D/I_G$ evolution, indicating the optimized nanotube-network order at 10 wt% SeCNT. **c** TGA curves confirming the presence of Sa and sericin coatings and the increased polymer-related weight loss with increasing SeCNT content.

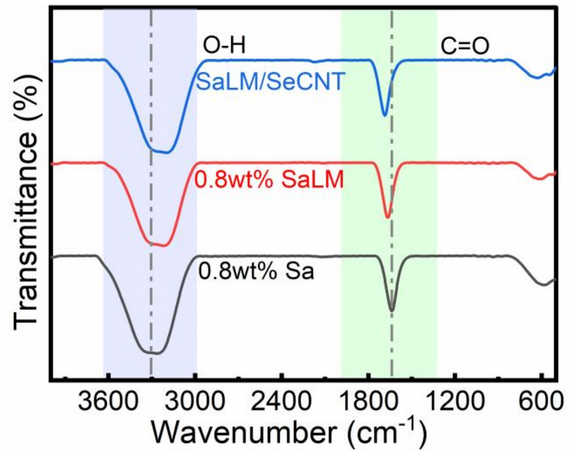


**Supplementary Figure 14. Comparison among Sa, SaLM and SaLM/SeCNT.** The FTIR spectra curves show that the secondary SeCNT coating preserves the inner SaLM crosslinked interface while introducing an outer nanotube network through hydrogen-bonding and π–π interactions.

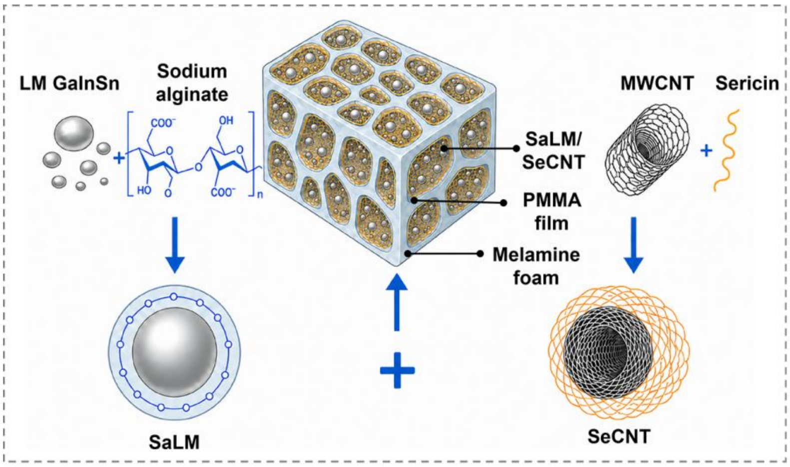


**Supplementary Figure 15. Schematic illustration of the PMMA-supported melamine-foam architecture, in which suspended PMMA interfacial films are formed across the foam pores and provide carrier surfaces for anchoring SaLM/SeCNT microdomains.**

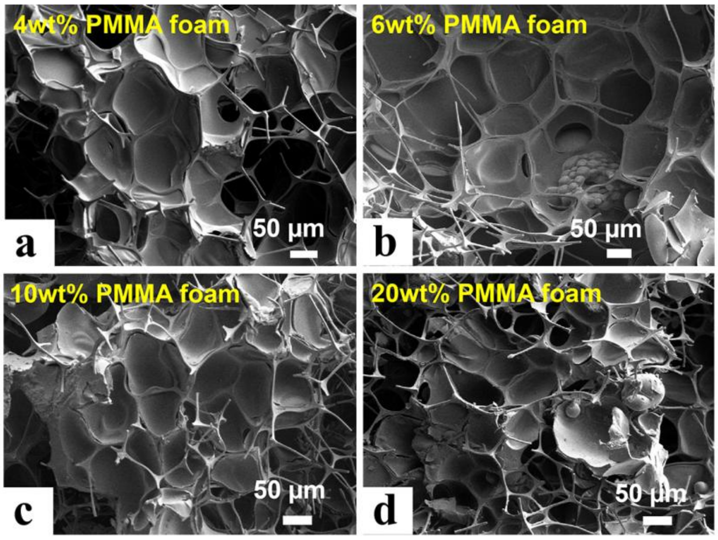


**Supplementary Figure 16. SEM images of melamine foams impregnated with different PMMA concentrations (4, 6, 10 and 20 wt%), showing the transition from discontinuous carrier films to overly thickened films.**

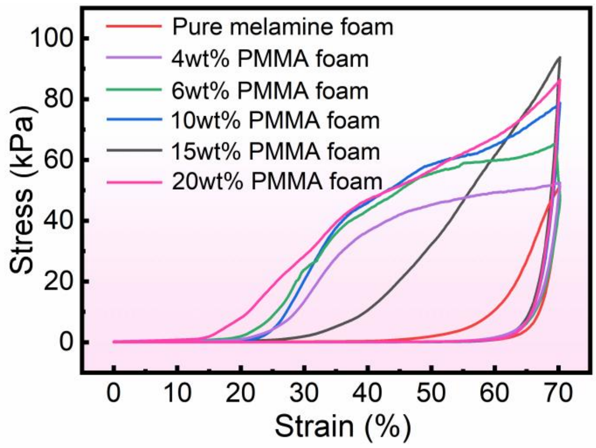


**Supplementary Figure 17. Compressive stress-strain curves of melamine foams treated with different PMMA concentrations.**

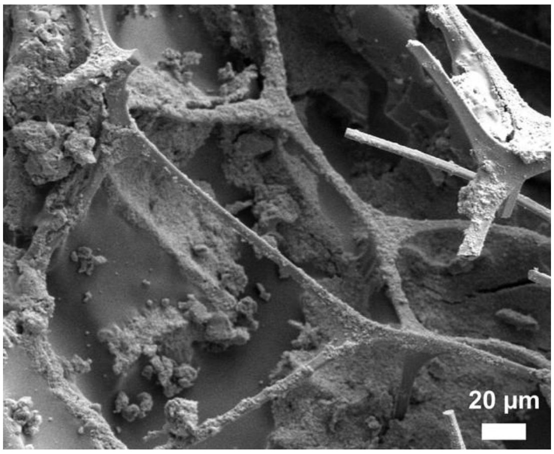


**Supplementary Figure 18. SEM image of SaLM/SeCNT-loaded melamine foam without PMMA treatment, showing skeleton-confined deposition of conductive complexes.**

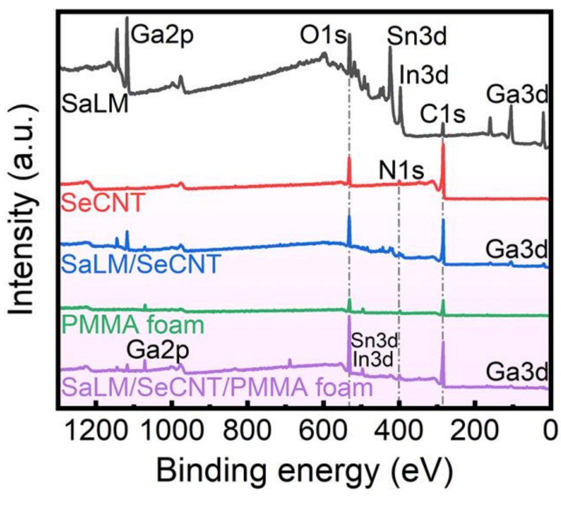

**Supplementary Figure 19. XPS survey spectra of PMMA foam and SaLM/SeCNT/PMMA foam, confirming the incorporation of Ga, In and Sn containing liquid-metal conductive complexes into the PMMA-supported foam.**

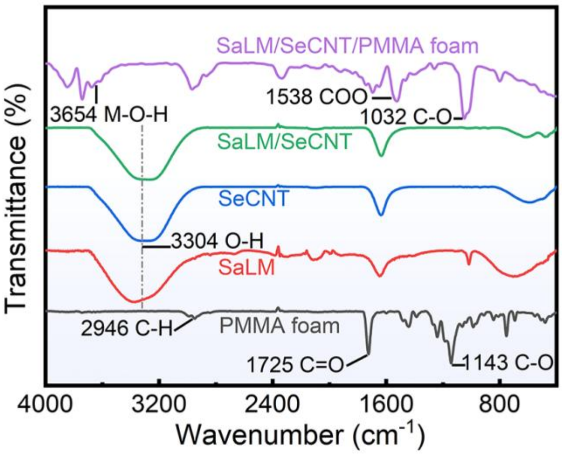


**Supplementary Figure 20. FTIR spectra of PMMA foam, SaLM/SeCNT droplets and SaLM/SeCNT/PMMA foam, showing shifts in C-O and O-H-related vibrations that indicate hydrogen-bonding and oxygen-containing interfacial interactions between PMMA and SaLM/SeCNT.**

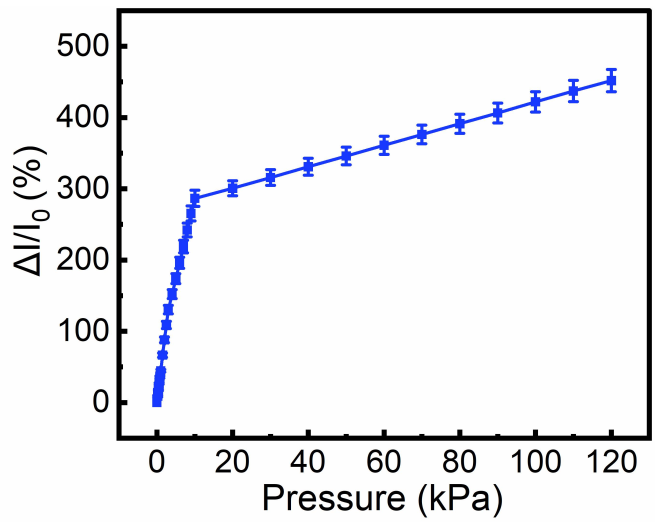


**Supplementary Figure 21. Reproducibility of the SaLM/SeCNT/PMMA foam pressure sensors.** Relative current responses from five independently prepared devices show small variation, with a relative standard deviation of 3.88%.

**Supplementary Table 3. Performance comparison between the recently reported liquid metal based pressure sensors and this work.**

| Materials | Structure | Fabrication method | Sensitivity ($kPa^{-1}$) | Detection range | Ref. |
|---|---|---|---|---|---|
| PDMS, EGaIn | Porous | Dissolving | 0.0014 | <20 kPa | 8 |
| TPU, EGaIn | - | Electrospinning | 0.324 | <50 kPa | 9 |
| PDMS, EGaIn | Pillar | UV laser etching | 2.07 | <135 Pa | 10 |
| MWCNT, EGaIn, PDMS | Hollow array | Demolding | 0.044 | <31 kPa | 11 |
| PDMS, EGaIn | Hierarchical structure | Self-sedimentation | 0.671 | <17 kPa | 12 |
| PDMS, EGaIn, Hydrogel | Microstructures and Bumps | Fs laser | 7.42 | <0.1 kPa | 13 |
| PDMS, GaInSn | Porous foam | Dissolving | 1.10 | <10 kPa | 14 |
| MWCNT, GaInSn, Foam | Porous foam | Dissolving | 41.94 | <1 kPa | This work |
| MWCNT, GaInSn, Foam | Porous foam | Dissolving | 21.25 | 1~10 kPa | This work |
| MWCNT, GaInSn, Foam | Porous foam | Dissolving | 1.61 | 10~120 kPa | This work |

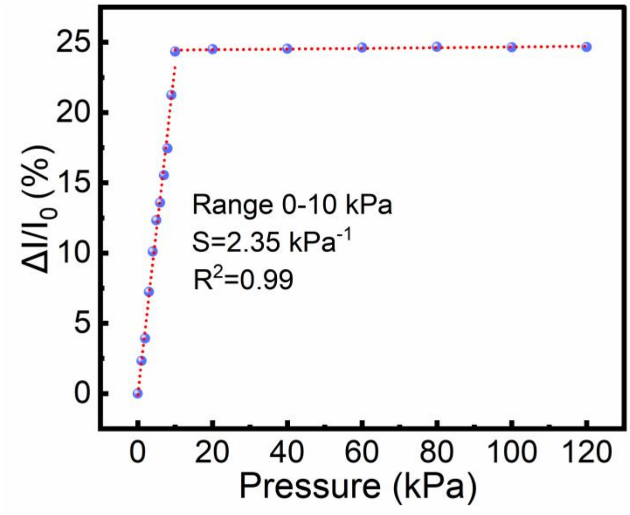


**Supplementary Figure 22. Pressure-response performance of the SaLM/SeCNT-loaded melamine-foam pressure sensor without PMMA carrier films, showing reduced sensitivity and a narrowed effective sensing range.**

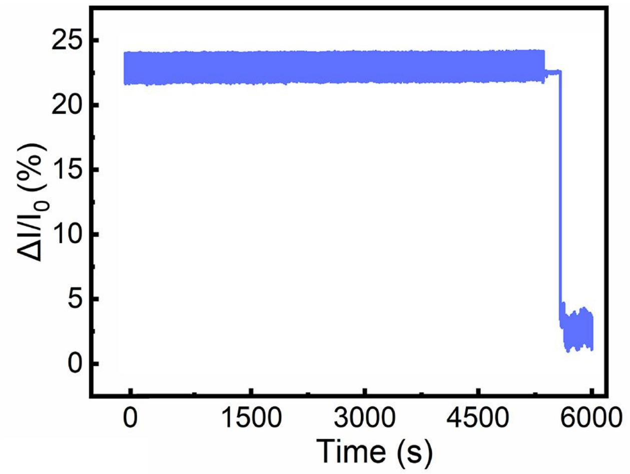


**Supplementary Figure 23. Cyclic response of the SaLM/SeCNT-loaded melamine-foam pressure sensor without PMMA carrier films, showing rapid signal degradation during repeated compression.**

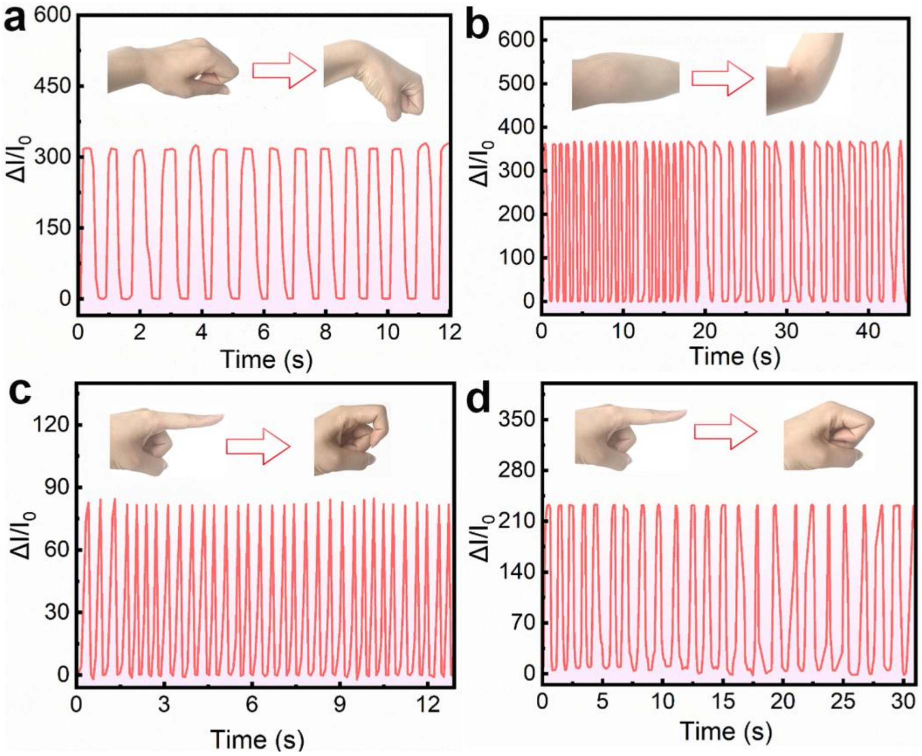


**Supplementary Figure 24. On-body motion monitoring using the SaLM/SeCNT/PMMA foam pressure sensor.** Representative signals recorded during wrist flexion, elbow flexion, and small- and large-angle finger bending demonstrate repeatable responses to both subtle and large human motions.

**Supplementary Figure 25. Full Morse-code chart used for tactile encoding.**

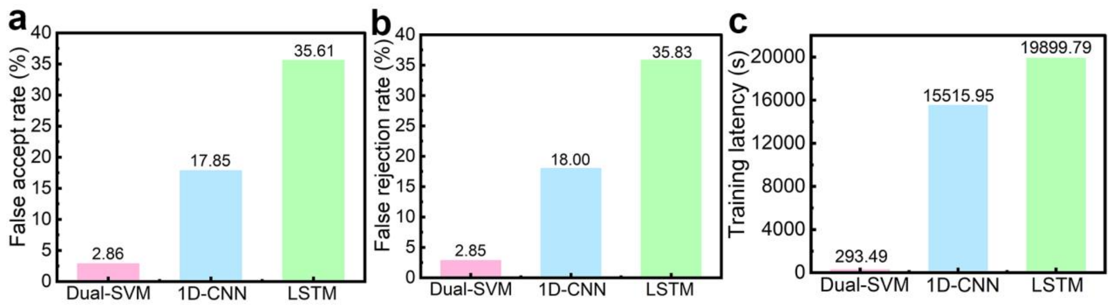


**Supplementary Figure 26. Authentication reliability and computational cost of the machine-learning models under the same hardware setting. a** FAR comparison among SVM, 1D-CNN and CNN-LSTM. **b** FRR comparison among SVM, 1D-CNN and CNN-LSTM. **c** Training-time comparison on Jetson Orin Nano.

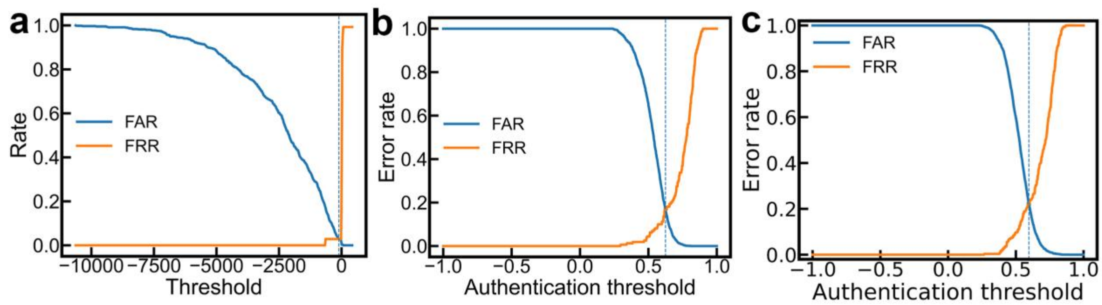


**Supplementary Figure 27. Threshold-dependent FAR and FRR curves for SVM, 1D-CNN and CNN-LSTM, showing the trade-off between accepting genuine users and rejecting impostor trials and supporting validation-set threshold selection.**

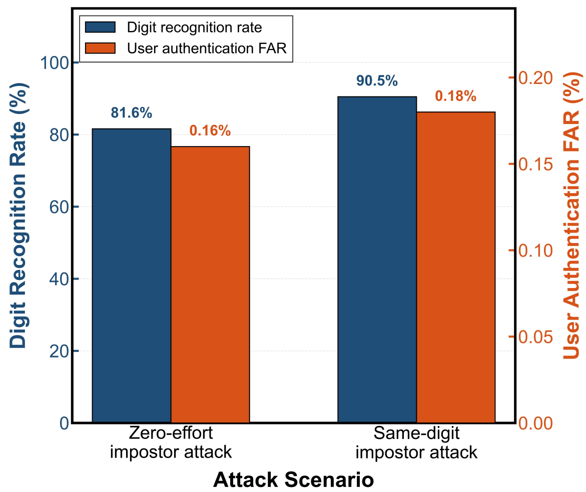


**Supplementary Figure 28. Performance evaluation of digit recognition and user authentication under distinct impostor attack scenarios.** The left vertical axis (deep navy bars) quantifies the digit recognition rate, while the right vertical axis (muted red bars) measures the user authentication False Acceptance Rate (FAR). Two threat models are evaluated on the horizontal axis: (i) Zero-effort impostor attack, and (ii) Same-digit impostor attack. The text labels explicitly denote the exact percentages for each metric.

**References**


1. Chen, W. et al. Directly printable and adhesive liquid metal ink for wearable devices. *Adv. Funct. Mater.* **35,** 2411647 (2025).

2. Ahmed, S., Momin, M., Ren, J., Lee, H. & Zhou, T. Self-assembly enabled printable asymmetric self-insulated stretchable conductor for human interface. *Adv. Mater.* **36,** 2400082 (2024).

3. Pei, D. et al. Self-assembled aqueous liquid metal inks for stretchable conductors and circuits. *npj Flex. Electron.* **10,** 7 (2026).

4. Zhang, M. et al. Versatile fabrication of liquid metal nano-ink based flexible electronic devices. *Appl. Mater. Today* **22,** 100903 (2021).

5. Wang, X. et al. Biocompatible collagen/liquid metal/carbon nanotube hydrogel for electromagnetic interference shielding in bioelectronics. *ACS Sens.* **10,** 8754–8763 (2025).

6. Chung, K. Y. et al. Naturally crosslinked biocompatible carbonaceous liquid metal aqueous ink printing wearable electronics for multi-sensing and energy harvesting. *Nano-Micro Lett.* **16,** 149 (2024).

7. Li, X. et al. Inter-skeleton conductive routes tuning multifunctional conductive foam for electromagnetic interference shielding, sensing and thermal management. *Nano-Micro Lett.* **17,** 52 (2025).

8. Xu, J. et al. Breathable encapsulated liquid metal foam-based soft stress sensor. *Adv. Mater. Technol.* **8,** 2201193 (2023).

9. Xu, H.-C. et al. All-fiber anti-jamming capacitive pressure sensors based on liquid metals. *Rare Met.* **44,** 4839–4850 (2025).

10. Han, K., Kim, I., Lee, E., Bae, G. Y. & Yang, C. Liquid metal composite-based flexible pressure sensors with high sensitivity. *ACS Appl. Mater. Interfaces* **17,**

40994–41001 (2025).

11. Xu, P. et al. Evaporation meets gravity: natural-force-driven fabrication of multifunctional flexible sensors for pressure, proximity, and material recognition. *Nano Energy* **146,** 111501 (2025).

12. Zhu, L. et al. Hierarchical structure by self-sedimentation of liquid metal for flexible sensor integrating pressure detection and triboelectric nanogenerator. *Adv. Funct. Mater.* **34,** 2400363 (2024).

13. Li, H. et al. Microstructured liquid metal-based embedded-type sensor array for curved pressure mapping. *Adv. Sci.* **12,** 2413233 (2025).

14. Chen, Z., Peng, H. & Zhang, J. An integrated electronic skin with biaxial sensitivity from a layered biphasic liquid metal/polymer film. *Mater. Horiz.* **11,** 4150–4158 (2024).